



HAL
open science

Transcranial ultrafast ultrasound localization microscopy of brain vasculature in patients

Charlie Demené, Justine Robin, Alexandre Dizeux, Baptiste Heiles, Mathieu Pernot, Mickael Tanter, Fabienne Perren

► To cite this version:

Charlie Demené, Justine Robin, Alexandre Dizeux, Baptiste Heiles, Mathieu Pernot, et al.. Transcranial ultrafast ultrasound localization microscopy of brain vasculature in patients. *Nature Biomedical Engineering*, 2021, 5 (3), pp.219-228. 10.1038/s41551-021-00697-x . hal-04062338

HAL Id: hal-04062338

<https://hal.science/hal-04062338v1>

Submitted on 20 Apr 2023

HAL is a multi-disciplinary open access archive for the deposit and dissemination of scientific research documents, whether they are published or not. The documents may come from teaching and research institutions in France or abroad, or from public or private research centers.

L'archive ouverte pluridisciplinaire **HAL**, est destinée au dépôt et à la diffusion de documents scientifiques de niveau recherche, publiés ou non, émanant des établissements d'enseignement et de recherche français ou étrangers, des laboratoires publics ou privés.



Distributed under a Creative Commons Attribution - NonCommercial - NoDerivatives 4.0
International License

1
2
3
4
5
6
7
8
9
10
11
12
13
14
15
16
17
18
19
20
21
22
23
24
25
26
27
28
29
30
31
32
33
34
35
36
37
38
39
40
41
42
43

Transcranial ultrafast ultrasound localization microscopy of the adult human brain vasculature

Charlie Demené*^{1,2}, J. Robin*^{1,2}, A. Dizeux¹, B. Heiles¹, M. Pernot¹, M.Tanter^{†1}, F. Perrent²

¹Physics for Medicine Paris, Inserm, ESPCI Paris, PSL Research University, CNRS

²Department of Clinical Neurosciences, HUG, LUNIC Laboratory Geneva Neurocenter, Faculty of Medicine, University of Geneva, Switzerland

* These authors contributed equally to this work.

† These authors contributed equally to this work.

Corresponding author: Mickael Tanter, Mickael.tanter@gmail.com

Abstract

Changes in cerebral blood flow are associated with pathologies such as stroke, aneurysms, neurodegenerative diseases and vascular cognitive impairment. Brain angiograms, typically performed via computed tomography or magnetic resonance imaging, are limited to millimetre-scale sampling and are insensitive to blood flow dynamics. Here, we show that ultrafast ultrasound localization microscopy of intravenously injected microbubbles enables the transcranial imaging of the deep vasculature in the adult human brain and the quantification of haemodynamic parameters, at microscopic resolution. We used adaptive speckle tracking to correct micrometric brain motion artefacts and ultrasonic wave aberrations induced during transcranial propagation, thus mapping the vascular networks of tangled arteries and the functional characterization of blood flow dynamics at a resolution of up to 25 micrometres. The increased resolution enabled the detection of blood vortices in a small deep-seated aneurysm, demonstrating that ultrafast ultrasound localization microscopy provides quantitative information unattainable with traditional angiographic methodologies. The technique may help improve the understanding of brain haemodynamics and the precision with which vascular abnormalities of the brain are related to neurological pathologies.

Ultrafast ultrasound localization microscopy of intravenously injected microbubbles enables the non-invasive imaging of the vasculature in the adult human brain and the quantification of haemodynamic parameters, at microscopic resolution

Obtaining functional information of living organs non-invasively across different scales is a major challenge of medical imaging research, as diseases often start locally at the cellular level before inducing large scale observable symptoms. Brain imaging adds another layer of complexity, as the organ relies on extremely complex, multiscale and interpenetrated networks of neurons, glial cells and vessels. Assessing brain vascular morphology and function is key of course for the diagnosis and monitoring of intracranial aneurysms, stenosis or arteriovenous malformations and for the management of acute stroke. It is also of interest for neurological pathologies, such as degenerative diseases¹, as there is increasing evidence for a close interaction between cerebrovascular diseases and cognitive impairment². In humans, most of this cerebrovascular imaging is performed using expensive, ionizing and/or invasive contrast injection dependent techniques, namely computed tomography

44 angiography (CTA) and magnetic resonance angiography (MRA). Furthermore, they are often limited
45 to an anatomical description of the vasculature at a millimetric resolution, and without capturing the
46 blood flow time dynamics relevant for assessing cerebrovascular function. No *in vivo* and *non invasive*
47 imaging technique has so far been proven able to capture anatomical *and* functional features below
48 the millimetric scale at the whole-brain level in humans. In this brain clinical imaging landscape,
49 contrast-enhanced ultrasound is marginally used. It is mostly performed through transcranial acoustic
50 bone windows (Figures 1a,b), if present, when imaging contrast of a regular Doppler examination is
51 too low, to monitor blood flow velocities in large cerebral basal arteries in the case of spasms, stenoses,
52 vascular malformations, dissections or after acute ischemic stroke. It is an easy-to-use, low-cost, widely
53 available bed-side method that shows hemodynamics in real time across the brain. However, its poor
54 spatial resolution and limited sensitivity still prevent contrast-enhanced ultrasound from being a
55 decisive imaging modality for cerebrovascular diseases.

56 The recent introduction of ultrasound localization microscopy (ULM) solved the conceptual
57 trade-off between spatial resolution and penetration depth while increasing sensitivity thanks to the
58 joint use of ultrasound contrast agents and ultrafast imaging. ULM relies on the same kind of concept
59 that has been the basis for the development of PALM³ (photo-activated localization microscopy) and
60 STORM⁴ (stochastic optical reconstruction microscopy) in optics: even if an imaging modality is
61 diffraction-limited, in the particular case of imaging an isolated object we can hypothesize that this
62 object is at the center of the diffraction spot. We can therefore localize it with a sub-resolution
63 precision that depends on the signal to noise ratio of the imaging device⁵. In the case of ultrasound
64 imaging, **these isolated objects consist** in diluted ultrasound contrast agents, and the method gains
65 from imaging at the fastest rate possible⁶. ULM demonstrated the unique ability of ultrasonic waves
66 to perform non-invasive deep microvascular imaging at the microscopic scale in rodents^{5,7-9}.

67 However, even though the ULM concept was introduced almost 10 years ago⁷, no translation of ULM
68 imaging to the human brain has been shown so far. Indeed the application of ULM to microvascular
69 brain imaging in humans faces major challenges, such as non-invasive brain accessibility, limited
70 acquisition time, transcranial propagation and brain motion. **Our group showed brain flow imaging in**
71 **humans without contrast¹⁰⁻¹³ using ultrafast Doppler Ultrasound, but never both transcranially and**
72 **with superresolution: it was either performed in neonates through the fontanel or in adults during**
73 **brain surgery (a result reproduced by Soloukey et al.¹⁴ in 2020) using an opened skull flap. Moreover,**
74 **imaging without contrast agent does not allow so far to beat the diffraction limit and would result in**
75 **the case of transcranial imaging to images with a resolution of the order of 1 to a few mm, 2 orders of**
76 **magnitude above ULM.** Imaging through the skull trans-temporally imposes the use of a small acoustic
77 aperture because the acoustic temporal bone window rarely exceeds 20 mm in diameter, and the use
78 of a low imaging frequency because the ultrasound attenuation coefficient in the skull is very strong,
79 and highly increasing with frequency: it scales in $f^{2.1}$ around 1MHz, 2.1 being the highest frequency
80 exponent of all biological tissues¹⁵. This large ultrasound attenuation is explained by two
81 mechanisms¹⁶: irreversible absorption in the bone and theoretically reversible diffraction effects due
82 to the speed of sound mismatch between the brain tissue ($\sim 1500\text{m}\cdot\text{s}^{-1}$) and bone ($\sim 3000\text{m}\cdot\text{s}^{-1}$) that
83 distorts the acoustic wave front (Figure 1c), a process called wave aberration^{17,18}. Finally, the influence
84 of motion artefacts highly escalates in the micrometric resolution range and is of first importance, as
85 ultrasound is traditionally handheld and as the brain moves inside the skull cavity.

86 In this paper, we demonstrate transcranial deep imaging of human cerebrovascular
 87 haemodynamics at the microscopic scale by jointly solving the major challenges of spatial resolution,
 88 skull bone aberration and motion artefacts for transcranial ULM. **We show that not only ULM is doable**
 89 **in human adults transcranially, but also that at this low ultrasound frequency, with an expected low**
 90 **SNR and in the presence of motion we could achieve resolutions of the order of 25 μm far beyond the**
 91 **typical 1 mm resolution of fUS imaging, a resolution never reached to our best knowledge by any other**
 92 **modality.** First, we used a phased array transducer of 19.2 mm acoustic aperture, driven at a 2 MHz

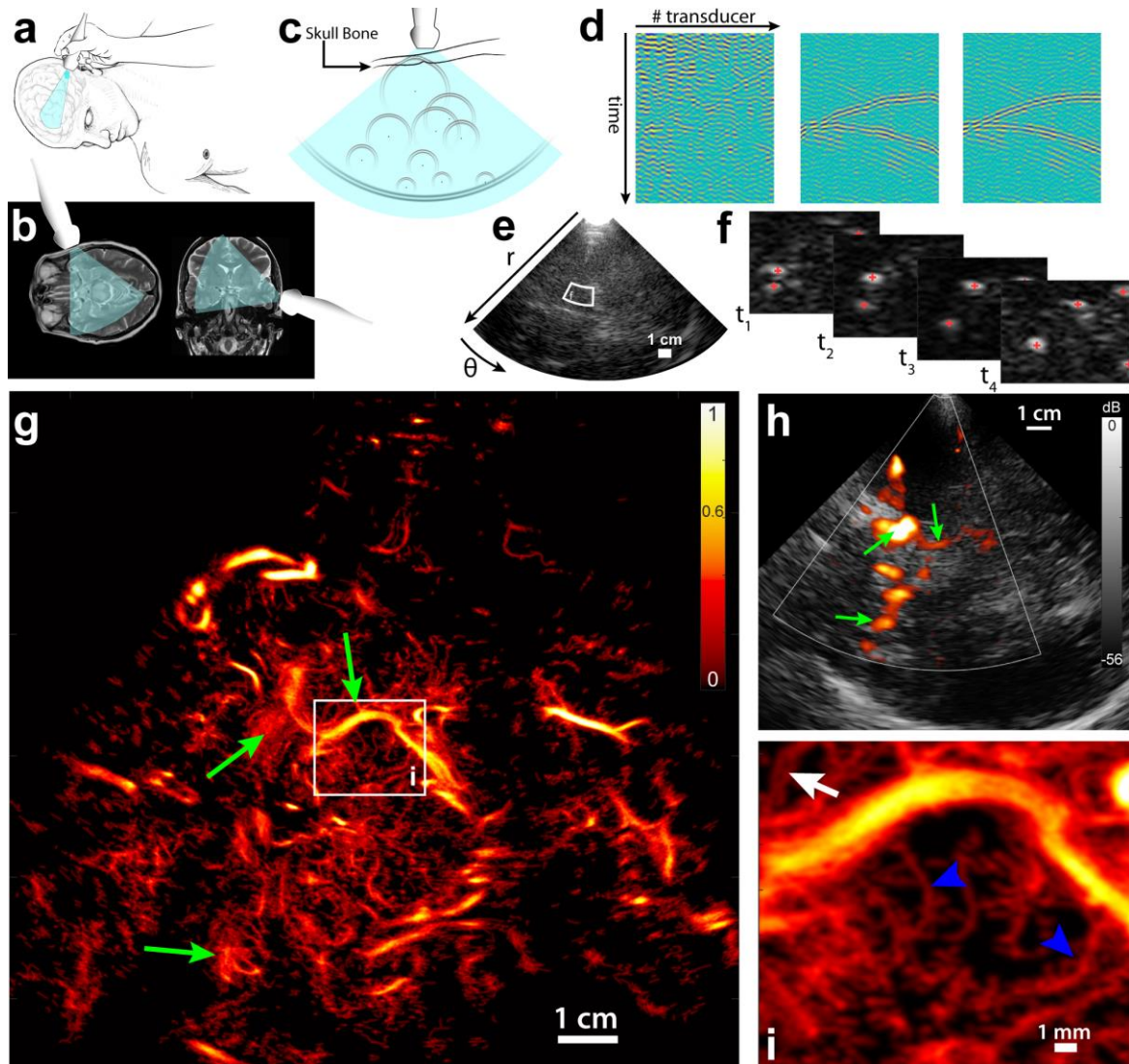


Figure 1: **a.** Positioning of the ultrasound transducer on the bone temporal window for brain imaging. **b.** Typical field of view in transverse and coronal brain sections. **c.** Diverging waves cover a wide field of view. Isolated microbubbles backscatter circular wave fronts toward the transducer array, which are distorted by the skull bone. **d.** Schematics of the aberration correction: (left) each transducer records the echoes backscattered from the brain, (middle) after singular value decomposition (SVD) filtering wave fronts from individual bubbles are visible and aberration law can be determined, (right) after time reversal of estimated aberration delays, bubbles echo returns to an expected hyperbola profile. **e.** After aberration correction, image reconstruction is performed on a polar (r, θ) grid. White box depicts zoomed area in **f.** After SVD filtering individual bubbles are localized, geometric centers are estimated and tracking of trajectories is realized. **g.** After the tracking of all bubbles in the field of view, a density map is reconstructed (using here 45 s of acquisition). White box depicts the zoomed panel **i.** Green arrows are landmarks to compare with **h.** **h.** Conventional Doppler image obtained in the same imaging plane as **g.** Green arrows are landmarks to compare with **g.** **i.** Zoom on a 15 x 17 mm area: small penetrating vessels of the mesencephalon are visible (blue arrows), and two very close vessels (350 μm apart) can be observed.

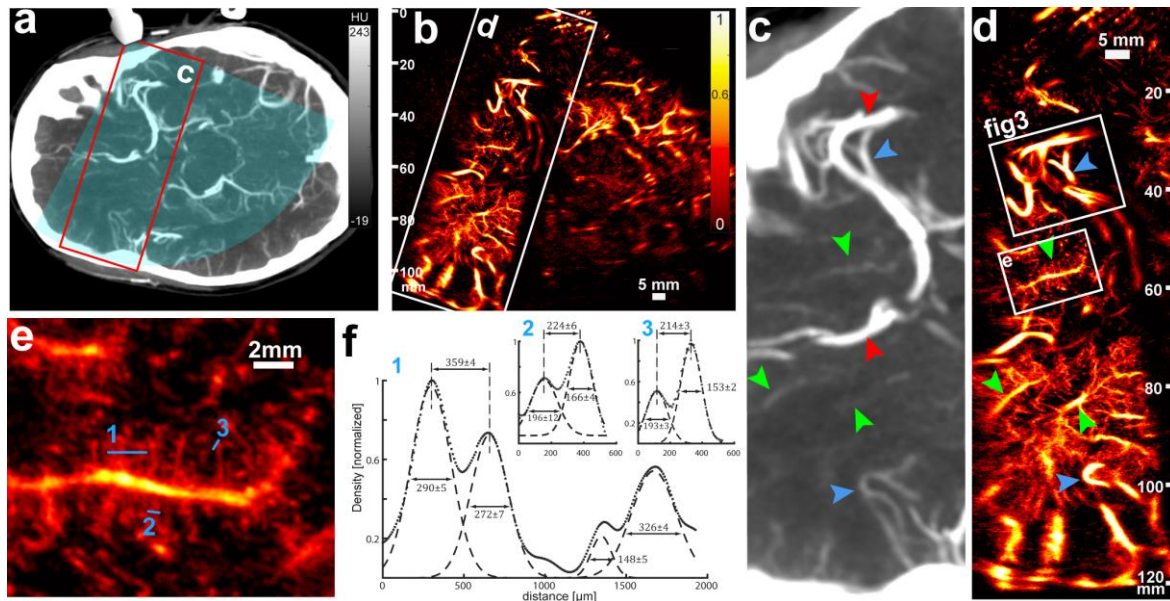


Figure 2: Estimation of the resolution in a standard imaging case. **a.** Patient brain axial CT scan section (6mm-thick slab) depicting the ultrasonic field of view (blue overlay) and the ROI in c and d (red rectangle). **b.** ULM image (2 min 15 s of acquisition) obtained in the same section, with the ROI in c and d. **c.** The CT scan shows the distal part of the middle cerebral artery (red arrow, top) and a segment of the anterior cerebral artery (red arrow, bottom). Very visible vessels (blue arrows) are also depicted as landmarks for visual comparison with ULM image d. Some structures are faintly observable (green arrows) **d.** ULM brain imaging in the same ROI (up to 120 mm depth). Blue and green arrows are the same landmarks than in c. Two ROIs (white boxes) are represented for further quantification in e and f and in figure 3. **e.** ROI (15 x 16 mm) delineating a small penetrating vessel and its radial ramifications. Numbered blue lines are used for cross section profiling in f. **f.** Cross sections of a wide set of vessels (1) and two pairs of close vessels (2 and 3). Dots represent the image data (see *Density and Velocity display* in M&M) (arbitrary unit) and dashed lines the Gaussian fit of the vessel cross sections. Inter-peak distance and full width at half maximum are given in μm with 95% confidence intervals.

93 central frequency: this choice corresponds to a trade-off (suppl Figure 1a-b) between emitting as much
 94 as possible within the transducer's available bandwidth (it is 1 to 5 MHz and central frequency is 3MHz,
 95 most available low frequency imaging transducers are not designed to efficiently emit ultrasound
 96 below 2 MHz), keeping the skull bone attenuation coefficient as low as possible^{15,19} (10 dB/cm at 1
 97 MHz, 40 dB/cm at 2 MHz, 60 dB/cm at 3 MHz) (suppl Figure 1a), targeting as much as possible an
 98 efficient backscatter coefficient for the contrast agent²⁰ ($\eta = 3.5 \cdot 10^{-3} \text{ cm}^{-1}$ at 1 MHz, $\eta = 8.9 \cdot 10^{-3} \text{ cm}^{-1}$ at
 99 2 MHz. $\eta = 1.2 \cdot 10^{-2} \text{ cm}^{-1}$ at 3 MHz), and keeping the highest possible resolution (at 2MHz, axial
 100 resolution to $0.82 \text{ mm} \pm 0.07 \text{ mm}$ and lateral resolution between 1 and 5 mm, depending on the
 101 imaging depth) (suppl Figure 1c-e). Then we implemented ultrafast ultrasound imaging²¹ using
 102 unfocused diverging waves, a technique that has previously been proposed for ultrafast cardiac
 103 imaging²² and been adapted here to human brain imaging. It uses the propagation of circular waves
 104 before recording the intracranial backscattered echoes. The patient is injected with small boluses (0.2
 105 mL) of contrast agents to attain a diluted concentration of microbubbles in the circulating blood. We
 106 chose a bolus dose that: - provided sufficient dilution for the microbubbles for individual identification,
 107 and enough concentration for an acquisition in a short time compared to what is described in the ULM
 108 literature – would allow for multiple injections in the case of probe repositioning – would remain in
 109 total lower than the maximum recommended dose of 2.4 mL^{23} .

110 The individual detection of each of these highly reflecting gas bubbles is exploited both for the
 111 correction of skull bone aberrations on the reflected wave fronts (Figure 1c, detailed in suppl. Figure
 112 2) and for subsequent super-resolution imaging of blood vessels. The recorded raw data corresponded

113 to a 2-dimensionnal (2D) spatio-temporal speckle pattern (schematized by Figure 1d, left), resulting
114 from the interference of ultrasonic waves backscattered from a random set of scatterers. In these data,
115 the tissue signal has a completely different spatial coherence signature as compared to the signal of
116 moving microbubbles. Using a spatio-temporal singular value decomposition filter²⁴ on these data
117 enables us to retain only the contribution of individual microbubbles (Figure 1d, middle). Therefore,
118 assuming the acoustic sound speed to be constant in the brain, the backscattered echo of an isolated
119 bubble will appear as a hyperbolic wave front in this particular space-time representation, with a slight
120 aberration due to the propagation through the skull bone. The aberration law is modelled as a near-
121 field phase screen introducing time delays on each element of the phased array^{25,26}. These aberration
122 delays are determined for typically 10^3 bubbles/s enabling averaging and local tuning (the same
123 aberration law is suited for a determined area of the image thanks to the isoplanatism approximation,
124 suppl Figure 2g), and used to correct for the aberration (Figure 1d, right, suppl. Figure 2h) before
125 beamforming the raw data into images on a polar grid (Figure 1e). Such adaptive beamforming
126 increases the number of microbubbles detected (increase between +5% and +13% if considering
127 bubbles whose track length are >10 frames, can be up to +43% when considering bubbles whose track
128 length are >30 frames, see Supplemental Figure 2j, and Supplemental Figure 2a-f for visual
129 comparison). The stack of resulting images is then filtered using a SVD spatio-temporal filter²⁴ to keep
130 only the microbubble signal (supplemental video), and the sub-pixel position of the microbubbles is
131 determined using a parabolic fit of local maxima for each image (Figure 1f). Trajectories are obtained
132 using a particle tracking algorithm²⁷ before building an image out of the positions of the microbubbles
133 in the entire field of view (Figure 1g, Supplemental movie): trajectories are interpolated so that each
134 pixel of the high resolution grid on the bubble trajectory is lightened up, before taking into account
135 the uncertainty of the bubble position by convolving this “bubble presence grid” with a Gaussian kernel
136 (whose spatial extent is function of the resolution). Microbubble positions are then corrected taking
137 into account motion artefacts estimated using phase correlation of ultrafast US data (Supplemental
138 Figure 3). In a 45 s acquisition, a 2D image revealing vascular structures with unrivalled sharpness can
139 be obtained. It shows for example very precisely part of the Willis polygon and the posterior cerebral
140 arteries, as can generally be observed with a conventional clinical ultrasound scanner with much lower
141 resolution (Figure 1h, green arrows). But most importantly, a very large number of small calibre
142 vessels, such as small ($\varnothing < 200 \mu\text{m}$) arteries penetrating the mesencephalon, can be visualized (Figure
143 1i).

144 Compared with a typical clinical contrast CT imaging (Figure 2a, c), transcranial ULM (t-ULM) shows
145 increased sensitivity and resolution (Figure 2b) at all depths (here up to 120 mm, which extend to the
146 contralateral cortex) (Figure 2d). Note that subtle anatomical differences may appear when comparing
147 the two images as the CT image represents a 6 mm constant thickness slab, whereas the thickness of
148 the ultrasound image varies in space due to elevation focalization²⁸. Our images have better quality
149 near 60-70 mm depth, as it corresponds to the elevation focus of the probe, and are degraded at large
150 depth due to the loss of this elevation focalization, and therefore of larger out-of-plane uncertainty on
151 the localization of the microbubbles. Attenuation is of course also a factor, but we can see in Figure 2d
152 that sensitivity is still good at 110mm (vessels are visible) while resolution is degraded (vessels are
153 blurry). The biggest vessels, such as the middle cerebral artery (MCA) or the anterior cerebral artery
154 (red arrows), as well as smaller branches (blue arrows), are visible in both modalities, but many
155 structures that are faintly captured by CT (green arrows) become clearly visible on t-ULM (Figure 2e),
156 with at least two more degrees of vessel branching delineated (supplemental Figure 4). At first glance,
157 the resolution increase compared to conventional ultrasound exceeds at least one order of magnitude
158 as neighbouring vessels that are estimated to be $214 \mu\text{m}$ apart at 60 mm depth can be evidenced from
159 this image (Figure 2f). However, quantifying the spatial resolution by resolving two nearest small

160 vessels is not an adapted approach as it is very unlikely to track a sufficient number of microbubbles
 161 flowing in two extremely close microvessels in the 45s acquisition time. Therefore, the proper
 162 estimation of t-ULM spatial resolution will be detailed further in the paper based on a *functional* rather
 163 than an *anatomical* definition.

164 Indeed, the sub-resolution positions can be used to build an anatomic t-ULM image, but more
 165 interestingly, these positions are part of a trajectory that provides each microbubble with an
 166 instantaneous 2D speed vector (Figure 3a) and reveal the flow dynamics. This enables us to build vector
 167 field maps of the flow velocity inside vessels of 1 mm diameter or less (Figure 3b). In Figure 3c, one can
 168 deduce from the very sharp change of direction that we are in the presence of two overlapping but not
 169 connected vessels, while it was not obvious on the anatomical-only image. Also, Figure 3d shows a
 170 turbulent flow in the turn of the U-shaped vessel, with a large variety of flow speed magnitudes across

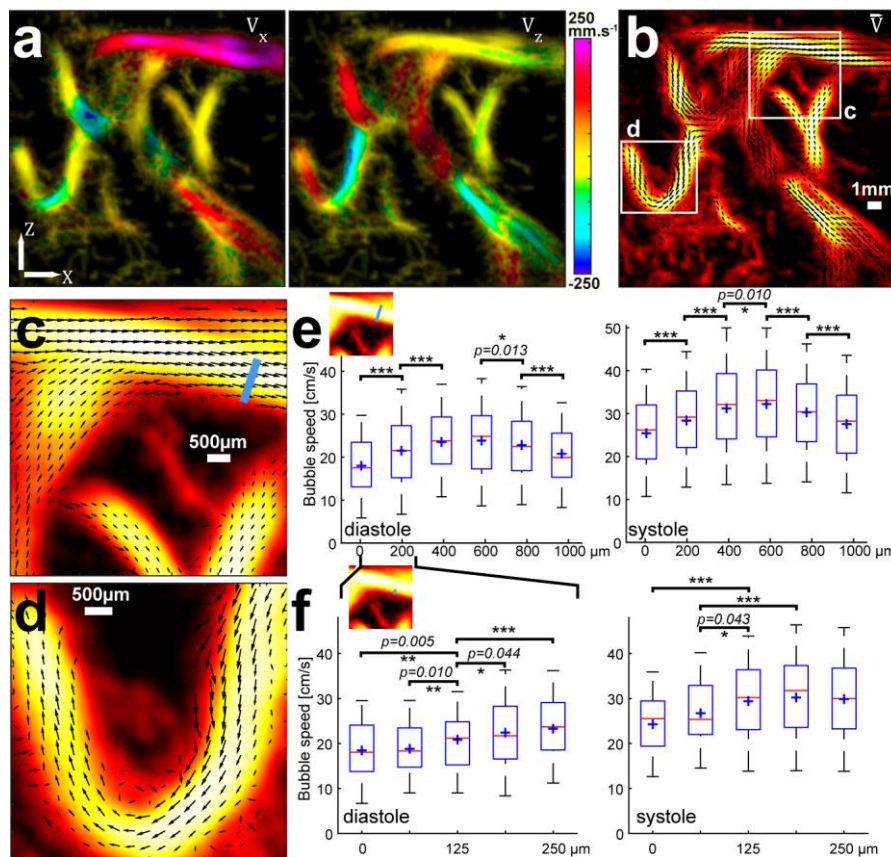


Figure 3: Estimation of the functional resolution. **a.** X and Z component of the speed vector extracted from the bubble trajectories overlaid on the density map. **b.** Combination of these two components enable quantitative representation of the flow vector fields inside those 1 mm wide cerebral vessels. Two ROIs are drawn for further zoom in **c** and **d**. **c.** A 6 x 6 mm ROI of the speed vector representation shows two superimposed vessels (top) (crossing without junction). The two bottom vessels, with lower flow speeds, are joining veins. **d.** A 5 x 5 mm ROI showing a sharp turn in an artery. The velocity profile across the vessel is very asymmetric due to the tortuosity of the vessel. **e.** Quantitative assessment of the velocity profile across the whole 1 mm section of the artery of **c**. (blue line in the thumbnail). Bubble velocities are gathered in 188 μm wide bins ($\lambda/4 \equiv$ diffraction-limited lateral resolution/8 at this depth); red central line indicates the median; boxes, 25th and 75th percentile; whiskers are $\pm 1.26 \sigma$ corresponding to 80% coverage in the Gaussian hypothesis (blue cross represents mean value). Significant differences in the mean value have been tested with $p < 0.05$ (*), $p < 0.01$ (**) and $p < 0.001$ (***). This quantitative velocity assessment has been done during diastole (left panel) and systole (right panel), showing largely increased bubble speeds during systole. **f.** The same quantitative assessment, on the extreme border of the vessel, on a 250 μm wide cross section (see thumbnail). Bins are now 62.5 μm wide ($\lambda/12 \equiv$ diffraction-limited lateral resolution/24 at this depth) and still show significant speed differences where the speed changes are the sharpest.

171 the vessel section due to the strong change of direction. We have quantified the functional t-ULM
172 resolution on a cross section of the vessel in Figure 3c, at 3 different scales (see *Flow quantification*
173 *and functional resolution estimation* in the Methods). When taking bubble speeds in 188 μm wide bins
174 along this 1 mm wide cross section it exhibits a typical parabolic blood flow profile with significant
175 speed differences (Figure 3e). Furthermore, this cross section flow speed analysis can also be
176 conducted at different moments in the cardiac cycle thanks to the very high temporal resolution of
177 ultrafast imaging (see *Motion detection and correction* in M&M), showing an increase of the central
178 median speed from 24.9 ± 6.2 cm/s in diastole (Figure 3e, left) to 33.1 ± 7.8 cm/s in systole (Figure 3e,
179 right). When looking at the vessel edge where the speed gradient is the sharpest (Figure 3f), it is
180 possible to exhibit significant differences on 62 μm wide bins both in systole and diastole,
181 corresponding to $\lambda/12$ (equivalent to conventional axial resolution/12 and conventional lateral
182 resolution /24 at this 38 mm depth, with a numerical aperture of 2, see suppl. Figure 1). When taking
183 25 μm wide bins, it is still possible to exhibit significant speed differences) near the edge of the vessel
184 but only in diastole, probably due to a more regular flow and a higher number of detected bubbles
185 (suppl. Figure 5). The maximum achievable resolution in the experimental conditions of the present
186 study is therefore 25 μm , but might be improved with longer acquisition time or more efficient
187 aberration corrections and motion compensation techniques.

188 In a 79-year-old patient (Supplemental Figure 6) presenting with an aneurysm on the distal part of the
189 right MCA, t-ULM using 24 s acquisition time (Figure 4a) showed an increased sensitivity and resolution
190 as compared to both CTA (Figure 4b) and time of flight MRA (Figure 4c). Common features, such as the
191 communicating posterior cerebral artery and part of the Willis polygon, can be observed (blue arrows),
192 but numerous other vessels invisible on those two major clinical modalities are unveiled, despite a very
193 short time of acquisition. The aneurysm is very obvious under the form of an excrescence at the
194 bifurcation of the right MCA (Figure 4a, green arrow) both in clinical images and on the t-ULM image.
195 But beyond this, t-ULM brings an exhaustive *functional* comprehension of the blood flow pattern inside
196 this aneurysm, when CT and MRI only give its anatomical description. Indeed, t-ULM reveals a small
197 vortex inside the left part of this aneurysm whose blood flow dynamics can be characterized thanks to
198 this 25 μm resolution (Figure 4 d–f, supplemental video). The potential for such imaging is hard to
199 predict, but it could be possible that the degree of clotting or the risk of rupture of a given aneurysm
200 might be influenced by the local fluid mechanics and blood flow speeds reached in the aneurysm.
201 Numerous studies try to link local flow mechanics, wall shear stress and health of the vessel wall^{29–31}.
202 Therefore such unique functional information could be of clinical relevance for making the decision
203 regarding surgical resection or coiling.

204 In a 63-year-old patient (Supplemental Figure 7) presenting with chronic cerebral hypoperfusion, right
205 posterior cerebral artery of foetal origin and an early occlusion of the right MCA that led to the
206 development of a complex local network of collateral arteries (Moya Moya³²-like disease), t-ULM
207 (Figure 4g) using 24 s acquisition time largely surpasses the CTA image (Figure 4h) in terms of sensitivity
208 (white boxes). While it is difficult to assess the functional efficiency of each of these collaterals on a CT
209 or MR image, it becomes very easy to understand where the flow is distributed with t-ULM thanks to
210 the capture of both flow speed and directions in all these vessels at microscopic scales (Figure 4i,j,
211 supplemental video).

212 By revealing both human cerebral vascular anatomy and flow dynamics at microscopic scales, t-ULM
 213 is very likely to become of major importance for the management of cerebrovascular diseases in the
 214 future. Its low cost, ease of use, sensitivity and quantification capabilities joined with almost two
 215 orders of magnitude improvement in terms of resolution as compared to current clinical modalities
 216 could disrupt the workflow of cerebrovascular patient management. One main limitation of this
 217 present study stands probably in the lack of real time processing for positioning the probe, this crucial
 218 positioning being performed using only the guidance of the B-Mode and conventional color Doppler.
 219 With our current ultrasound machine, raw data are saved to disk for off-line processing due to limited

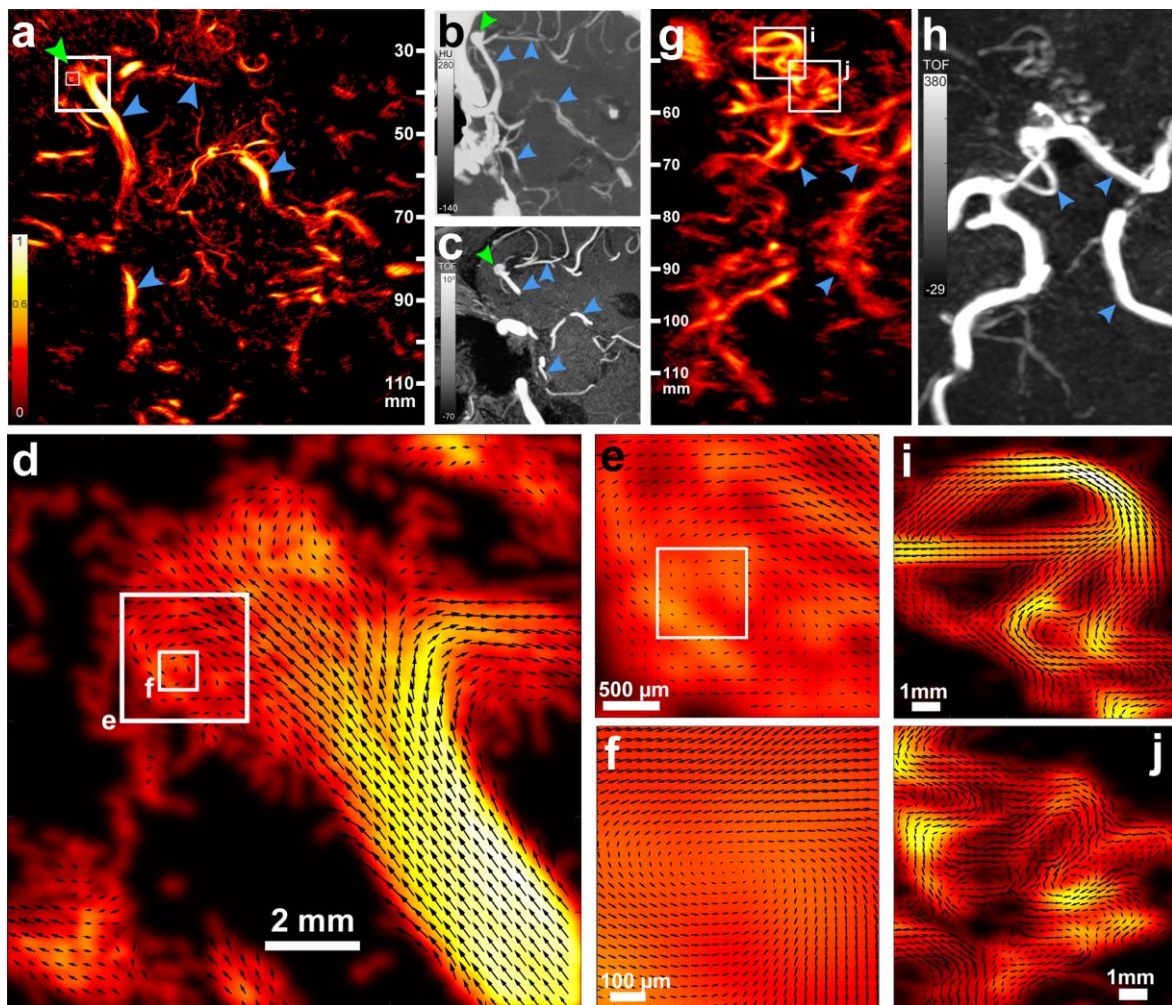


Figure 4: Clinical relevance of transcranial ULM. **a.** ULM (24 s of acquisition) tilted axial brain section of a patient diagnosed with an aneurysm (green arrow) in the right MCA. Blue arrow depicts vascular landmarks visible on CT and MR images for the reader's sake. The three white boxes correspond to the enlarged images of d–f. **b.** Maximum intensity projection of a 6 mm thick CTA slab corresponding to the ULM imaging plane. **c.** Maximum intensity projection of a 7 mm thick MRA slab corresponding to the ULM imaging plane. **d.** A 12 x 12 mm ROI on the MCA aneurysm depicting the local flow vector field. The longest arrow corresponds to a 20 cm/s speed, values above 20 cm/s are clipped. **e.** A 2.5 x 2.5 mm ROI on a flow vortex inside the aneurysm. **f.** Further zoom on an 800 x 800 μm ROI centered on the vortex, showing almost null velocity at the center. Longest arrow corresponds to a 5 cm/s speed, values above 5 cm/s are clipped **g.** ULM (24 s of acquisition) brain section of a patient presenting with an occlusion of the right MCA, resulting in the abnormal development of a large number of collateral arteries (white boxes). Contralateral side is visible for visual comparison. **h.** Maximum intensity projection of a 10 mm thick CTA slab corresponding to the ULM imaging plane, where these collateral arteries are faintly observed and without functional information (flow). **i.** and **j.** ROIs (10 x 10 mm) on these collateral arteries depicting the direction and magnitude of the flow, stop points and bifurcations, enabling functional quantification. Longest arrow corresponds to a 20cm/s speed.

220 computation capabilities and fine tuning of image reconstruction parameters. Currently, calculations
221 are performed on a regular computer (Intel® Xeon® CPU E5-2630 @2.40 GHz, NVidia GeForce GTX
222 Titan X) with limited optimization (mostly Matlab® code), and typical post processing time for 1s of
223 acquisition is: beamforming + aberration correction (8 s + 45 s + 8 s), filtering (0.5 s), localisation (45
224 s), bubble tracking (1 min). The two last operations are non-optimised matlab based calculations that
225 can be heavily accelerated. In particular localization is heavily parallelizable as it is image independent,
226 and bubble tracking can be done in parallel on image sub-patches, which would drastically reduce the
227 calculation time as it is non-linear with the number of bubbles considered. Real time t-ULM displays
228 (or at least partial displays) would enable to tackle less obvious cerebrovascular pathologies, such as
229 very small aneurysms, stenoses or defects in small vessels. These aspects are only due to the
230 computational power available on our scanner and real time displays will be achievable in the next few
231 years.

232 It is difficult to infer the success rate of t-ULM based on our present study **compared to color Doppler**
233 **imaging**³³, as we need a larger cohort. In Europe, so far, Sonovue® is routinely used in neurosonology
234 in order to image difficult patients (absence of temporal bone window), with a good success rate, but
235 it is difficult to foresee how the precision of t-ULM will be patient-dependent. Sonovue® has been
236 approved in more than 40 countries, is widely used in Europe for various imaging applications. It is
237 routinely used for transcranial ultrasound Doppler imaging in a lot of European countries such as
238 Germany, Switzerland, Portugal or France. It has been approved in the US under the name LUMASON
239 for echocardiographic and liver imaging applications both in adults and children, underlining its
240 innocuousness. As transcranial color-coded ultrasound is only performed in a very few specialized
241 medical centers in the US, SonoVue/LUMASON is not registered for this application. Nevertheless, the
242 concept of ULM should be applicable to any other approved contrast agents (Optison, Levovist,
243 Definity).

244 One important limitation of our work is the limited access provided by the temporal sutures through
245 which sound can enter the brain. This was actually a deliberate choice to choose an ultrasonic probe
246 and a hardware setup as close as possible to what is already available in the clinics. The obtained
247 images show very good delineation of the central cerebro-vascular structures, but maybe with a
248 slightly lower central frequency and deeper elevation focus we could envision good delineation of the
249 cortical structures from the contralateral temporal window, and therefore whole brain imaging using
250 both temporal windows. However, we could also imagine lifting the temporal access constraint by an
251 important technological development involving much larger transcranial matrix probes working at
252 lower frequency. By taking into account the skull bone attenuation coefficient and the backscatter
253 coefficient of Sonovue® (suppl Figure 1a), there could be a huge advantage at developing large
254 ultrasonic helmets working at low central frequency of 1MHz or below. Simulating the relative receive
255 signal amplitude when using Sonovue microbubbles and propagating back and forth through 1cm of
256 skull bone, there is a typical 50 dB difference between working at 2 MHz and 1 MHz (F.J. Fry and J.E.
257 Barger, 1978). There will of course be a small loss of resolution, but that might be largely compensated
258 by the much larger apertures, as the temporal window would not be a constraint anymore. Also,
259 working on contrast agents with a peak of backscatter coefficient at lower frequency might be of
260 interest.

261
262 3D t-ULM imaging would also be of major interest in particular for screening. There is no impediment
263 to it as proofs of concept of 3D ULM in flow phantoms were recently published³⁴. 3D t-ULM imaging
264 would probably reduce the examination time, operator dependence and injected doses of
265 microbubbles, improving the workflow of the clinicians. Beyond clinical applications, the ability of t-
266 ULM to reveal human cerebrovascular dynamics at microscopic scales will profoundly expand our
267 fundamental understanding of brain vascular function and dysfunction.

268 **Materials and Methods**

269 ***Patient management and safety of imaging protocols***

270 All experiments strictly complied with the ethical principles for medical research involving human
271 subjects of the World Medical Association's Declaration of Helsinki. Healthy volunteers and patients
272 were recruited from the ambulatory consultation unit and from the stroke unit/neurovascular ward
273 after giving informed and written consent according to the imaging protocol approved by the ethical
274 committee of Geneva (CCER 2017-00353). By minimizing the dose of injected contrast agent to the
275 minimum enabling the ultrasound localization microscopy and by minimizing the amplitudes and
276 durations of the ultrasound exposures, the imaging sessions followed the ALARA principle. These were
277 largely below the FDA recommendations (AUIM/NEMA 2004, Track 3) for ultrasound imaging, with a
278 maximum mechanical index (MI) of 0.46 (FDA recommended maximum value is 1.9), a maximum
279 derated spatial peak temporal average intensity (ISPTA) of 64.3 mW/cm² (FDA recommended
280 maximum value is 720 mW/cm²) and a maximum thermal cranial index (TIC) of 1.99 (no
281 recommendation but FDA regulations ask for an explanation for values above 4).

282 The overall aim of the study and procedures were explained to the patients before procurement of the
283 informed and written consent. An intravenous cannula was placed in the medial cubital vein for
284 subsequent injection of ultrasound contrast agents (SonoVue, Bracco, Italy). SonoVue® (8
285 microlitres/ml powder and solvent for dispersion for injection) is an ultrasound contrast agent
286 consisting of a suspension of tiny microbubbles (most microbubbles between 2 and 9 microns) with a
287 unique structure made of an inert gas, sulphur hexafluoride, and a phospholipid shell that provides
288 stability and prevents microbubble coalescence. When injected intravenously, SonoVue® strongly
289 enhances the echogenicity of blood, which results in an improved signal-to-noise ratio. It is commonly
290 used in many European countries when the temple acoustic window does not allow good visualization
291 of the intracranial vessels. It is quickly eliminated from the bloodstream in the lungs (EMA / 502204)³⁵
292 with a mean terminal half-life of 12 min. The use of second-generation echocontrast agents, such as
293 SonoVue, is approved in Europe for cerebrovascular applications in humans (European medicine
294 agency decisions EMA / 502204 / 2015 & EMEA / H / C / 000303).

295 ***Safety measurement procedures***

296 Ultrasonic amplitudes and durations were evaluated using certified Acoustic Measurement Tank and
297 its software (Acertara, Colorado, USA), following the provided calibration procedures. After probe
298 alignment in the depth direction, a Z-scan was performed in the aperture's centre to obtain the
299 pressure profile. Raster scans were then done in three depth positions (1) Z = 0.5 cm, 2) Z = 1 cm and
300 3) Z = 6.5 cm), respectively, corresponding to measurements 1) in the near field at the skull location,
301 2) just behind the skull and 3) at the probe elevational focus. The regulation indices (MI, ISPTA, and
302 TIC) were then measured at each depth position (including measurement of the maximum peak
303 negative pressure in the radiated ultrasonic field for MI and ISPTA calculations, and integration of the
304 ultrasonic energy over the ultrasonic field spatial extent at each depth for TIC calculations), before
305 using the maximum value over the three depths for each regulation index. Maximum MI was 0.465 (at
306 0.5 cm, value 0.202 at 6.5 cm, measured in water, will be highly mitigated by the presence of the skull
307 (typically divided by a factor 5.6 if we consider a 15dB attenuation due to 0.5cm of skull bone)) (FDA
308 recommendation is < 1.9) and maximum derated (-3 dB/cm) ISPTA was 64.3 mW/cm² (FDA
309 recommendation is < 720 mW/cm²). Those values measured in water are probably much lower when
310 imaging the patient due to skull bone attenuation. Thermal indices were also calculated and reached
311 maximum values of 1.49 (TI soft tissue), 1.9 (TI bone) and 1.99 (TI cranial), largely below the limit of 4
312 recommended by the FDA (values above 4 are possible but should be explained). The TI is defined as
313 $TI = W_p/W_{deg}$, where W_p is the relevant (attenuated) acoustic power at the depth of interest, and

314 W_{deg} is the estimated power necessary to raise the tissue equilibrium temperature by 1°C according
315 to a chosen specific tissue model.^{36,37} Therefore, a TI value of 2 would correspond to a 2°C increase in
316 equilibrium temperature assuming a worst case scenario. In our case the most important index is the
317 cranial TI (TIC), and it largely overestimate the temperature rise as it is designed for continuous
318 ultrasound imaging, while in our case ultrasound is on only half of the duration of the examination (1s
319 of acquisition, 1 s of pause).

320

321 **Ultrasonic sequences**

322 Ultrasonic acquisitions were performed using an ultrafast programmable scanner (Aixplorer,
323 Supersonic Imagine, Aix en Provence, France) and a phased array ultrasonic probe (XP 5-1, Supersonic
324 Imagine) (central frequency 2.93 MHz, 90% bandwidth at -6 dB, pitch 0.2 mm, 96 elements). Ultrafast
325 ultrasound imaging sequences consisted of the emission of diverging waves coming from four virtual
326 sources regularly spaced (every 3.2 mm) placed 11.44 mm behind the transducer array (giving a 80°
327 angular field of view). Choice of the central frequency was based on an optimization on 3 parameters
328 whose evolution vs frequency is given in suppl Figure 1a : available transducer bandwidth (given by
329 the transducer constructor), skull attenuation coefficient α_{skull} (adapted from Bamber et al¹⁵) and
330 Sonovue® backscattering coefficient η (adapted from Schneider et al²⁰). Supplemental Figure 1 b shows
331 in black the curve combining those parameters (BW is squared as the signal **passes** through the
332 transducer at emission and at reception, α_{skull} is actually calculated for a total distance of skull
333 propagation of 1 cm (0.5 cm thickness back and forth, this length actually **does** not influence the
334 position of the peak), the backscatter coefficient η is taken as a square root as it **comes** from a power
335 measurement and we are considering amplitude of the received signal). Supplemental figure 1 b shows
336 in red the spectrum of the 2 MHz-2 cycle-squared electric pulse sent from the ultrasound scanner to
337 the ultrasound transducer: it fits nicely above the black curve, we chose a slightly higher frequency in
338 order to keep as much resolution as possible, it is a squared signal as this is the kind of signal that
339 ultrasound pulsers are able to emit. Therefore ultrasonic pulses consisted of two cycles centred at 2
340 MHz, fired at the maximum pulse repetition frequency allowed by the desired imaging depth (typically
341 4900 Hz) by groups of four pulses (for the four sources), repeated at a “frame rate” of 800 Hz (“frame
342 rate” means at which frequency compound frames made of the 4 different virtual sources of
343 insonification are outputted) during 1 s. For each pulse, backscattered echoes were recorded by the
344 transducer array, digitalized at 200% bandwidth (meaning four samples per wavelength), and stored
345 in a so-called radiofrequency (RF) data matrix. These RF data matrices are the starting point of
346 aberration correction and image reconstruction. This operation was repeated every 2 s, which is the
347 fastest sequence rate achievable by our system at this point that enables to save on the enormous
348 amount of data to disk (several Gb/s) for further processing. **To summarise: for 1s, the ultrasound is**
349 **on and both pulsing diverging waves at 4900Hz and acquiring data, for 1s, the ultrasound is off and**
350 **saving the RF data that were just acquired to disk**, and this process loops during a desired duration (45
351 s for patient of figure 1, 2 min 15 s for patient of figure 2 and 3, 24 s for patients of figure 4).

352

353 **Aberration correction and beamforming procedures**

354 The correction of skull bone aberrations induced during transcranial propagation can be done in a two-
355 steps approach as already discussed *ex vivo*³⁸⁻⁴⁰. First, we analyse the wavefront reflected by individual
356 microbubbles acting as point-like sources in the medium. This reflected wavefront corresponds to the
357 exact Green’s function relating the source location to each element of the ultrasonic array and can be
358 used to measure the skull aberration. Secondly, the time reversed version of this aberration law
359 (corresponding to the temporal delays induced by the skull bone during the backward propagation) is
360 introduced as a time shift correction on each element of the array before reprocessing the
361 beamforming of the raw ultrasonic data and produce corrected ultrasonic images. SVD clutter filtering

362 was performed on the RF data matrices to remove tissue signal and isolate wave fronts coming from
363 individual microbubbles. Uncorrected images were reconstructed from these filtered RF matrices using
364 delay-and-sum beamforming on a polar (r, θ) grid with classical spherical delays, and bubble positions
365 corresponding to the isolated wave fronts were stored, along with the forward and return spherical
366 delay laws associated with these positions. For each considered bubble, the forward delay law was
367 used to virtually focus the filtered RF signals from the four diverging wave emissions on the bubble
368 location, and the return delay law was then used to flatten the isolated wave front. The phase
369 aberration profile was calculated via cross-correlation, as the remaining relative delays appeared in
370 the wave front across the transducer elements. Measurement of the spatial coherence of the wave
371 front was used as a metric for convergence, and only the bubble positions that encountered an
372 increase of this coherence **through** this iterative process were kept until the end.

373 Phase aberration laws were compared over the whole image to determine isoplanatic regions within
374 which the aberration could be considered constant (variations across bubbles $< T/8$). Individual bubble
375 aberration laws were averaged within each of these regions, and corrected images were reconstructed
376 from raw RF data using regionally-corrected delay laws in a delay-and-sum beamforming on a polar
377 (r, θ) grid.

378 ***Motion detection and correction***

379 Tissue motion within 1 s stack of images was estimated using cross-correlation techniques already
380 described for ultrasonic tissue displacement or strain estimations^{41,42}. Briefly, estimation of the inter-
381 frame axial displacement was obtained by multiplying the in phase-quadrature content of one pixel by
382 the complex conjugate content of the same pixel in the subsequent frame. This was done for all pixels;
383 a 3 x 3 pixel averaging filter was used before estimating the phase of the complex in each pixel, being
384 proportional to the inter-frame displacement. This displacement was also used to detect the systole
385 time point, as the tissue motion will be larger and exhibit a distinct peak during the systole. Therefore,
386 each microbubble spatial position was accompanied by a time position relative to the systole position,
387 enabling discrimination between systole and diastole. This will be used for further intra-cardiac cycle
388 speed analysis. Motion between 1 s blocks was estimated as a 2-fold process: first, by calculating the
389 affine transformation matrix between the corresponding Power Doppler images before localization
390 processing (pre-registration) and then by computing the fine transformation matrix on density images
391 after localization microscopy processing of those images already pre-registered. Effect of the motion
392 correction can be appreciated on Supplemental Figure 3.

393 ***Localization microscopy data processing***

394 Beamformed IQ data were filtered using the SVD spatio-temporal filter described by Demené et al.²⁴
395 (between 35 and 60 singular values were removed depending on the level of tissue motion) to remove
396 tissue signal and keep only the signal from the moving scatterers (the microbubbles). Magnitude of
397 the filtered IQ signal was kept and formed a stack of images depicting the individual motion of bubbles.
398 A binary mask was built based on the vesselness filtering^{43,44} (implementation available on Mathworks
399 file exchange, ©Dirk-Jan Kroon 2009, and © Tim Jerman, 2017) of this stack of images. The vesselness
400 filter belongs to a particular family of image processing filters optimised to improve contrast of vascular
401 structures in 2D or in 3D, that are particularly suited for example for improvement of vascular imaging
402 of the retina (2D) or for improvement of 3D CT angiography. They relies on the eigen decomposition
403 of the Hessian matrix. The Hessian matrix is defined as the convolution between the image intensity
404 (can be 3D) and the second derivative of a Gaussian kernel, therefore it approximates a 2nd order
405 derivative at a certain scale⁴⁵. Taking into account the relative sign and magnitude of the eigen values
406 of this Hessian matrix within an “enhancement function” enables to identify certain types of structures

407 (namely plate-like, tubular, blob-like). The vesselness filter is based on a certain formulation of this
408 enhancement function, several formulations having been proposed in the past like Frangi, Sato, Li,
409 etc⁴⁴. This type of filter is efficient in our case as bubbles moving in time will appear in a 3D matrix
410 (space x space x time) as tubular (vessel-like) structures, and therefore will be enhanced using a
411 vesselness filter in 3D. Both image stack and mask stack were interpolated (Fourier space based
412 interpolation for the image stack and nearest neighbour interpolation for the binary mask) down to a
413 radial resolution $dR = \lambda/6$ and an angular resolution of $d\theta = 0.5^\circ$. Local maxima detection was then
414 performed within the masked area for each 2D image of the image stack. These local maxima are locally
415 correlated with a typical point spread function (imaging response of an isolated microbubble) modelled
416 as a Gaussian spot of axial dimension λ and lateral (angular) dimension of $\arctan(\frac{\lambda}{d})$, and local maxima
417 with weak correlation (< 0.6) were discarded (local spatial speckle fluctuation can generate local
418 maxima but are not like a point spread function). Sub-pixel maxima localization was then performed
419 using a fast local (5 x 5 pixel neighbourhood) 2nd order polynomial fit. Maxima positions were then
420 converted from polar to Cartesian coordinates. Tracking of the maxima positions was performed using
421 a classical particle tracking algorithm⁴⁶ (simpletracker.m available on mathworks ©Jean-Yves Tinevez,
422 2019, wrapping matlab munkres algorithm implementation of ©Yi Cao 2009) with no gap filling and
423 maximal distance linking of 1 mm (corresponding to a bubble maximum speed of 80 cm/s). Bubble
424 tracks shorter than detected positions were removed, which was based on the idea that microbubbles
425 should be observed in several consecutive frames, enabling us to drastically reduce the level of false
426 bubble detection. The successive positions gathered in one track were used to compute the interframe
427 bubble velocity vector components V_x , V_z and velocity magnitude $\|\vec{V}\|$. The successive positions were
428 also used to compute a curvilinear abscissa along their trajectory in order to interpolate both positions
429 and speeds at a smaller space step (0.01 mm).

430 ***Density and Velocity display***

431 Compared to ULM maps obtained by others^{46,47} in animals in very controlled conditions and non-
432 transcranially, the data obtained in our paper were acquired in a very short time (between 24 s and 2
433 min 15 s) to minimize discomfort for the patient and in challenging conditions (motion, handheld
434 probe, and skull aberrations). Therefore, we had to make the most of all the bubbles detected during
435 the acquisition to build a vascular map as representative as possible of the underlying vasculature.
436 Therefore, images were built based on a position map (made of very small dots in a 0.01 mm regular
437 grid) convolved with a Gaussian kernel whose standard deviation equals the best resolution achieved
438 in this paper (i.e., 62 μm). This visually enhances the resulting image by smoothing vessels as compared
439 to building and imaging them directly on a 0.062 mm grid.

440 Velocity vector fields were obtained on a regular grid via bilinear interpolation of the irregularly
441 distributed microbubbles vector speed. These vector fields were also spatially filtered using a Gaussian
442 kernel ($\sigma = 62 \mu\text{m}$). This enables us to display the velocity components of Figure 3b and subsequent
443 vector field images.

444 ***Flow quantification and functional resolution estimation***

445 For quantification on cross axis speed profiles, the speeds of individual bubbles were binned along a
446 vessel transverse section (bubbles inside 1 mm longitudinal extent), before statistical testing (ANOVA
447 with post hoc t-test with Bonferroni correction). Bins were 188 μm , 62.5 μm (Figure 3) and 25 μm
448 (Suppl. figure 4) wide. Were retained bubbles whose trajectories were within 1 mm on either side of
449 the cross section. Bubbles were considered in systole when within 0.3 s around the systolic peak speed
450 and in diastole when within 0.6 s around the diastolic minimal speed. For the 188 μm bins (6 bins),
451 speed differences were estimated on (N=46, N=146, N=215, N=194, N=130, N=82) bubble trajectories

452 representing respectively (242, 1057, 1710, 1698, 1009, 579) bubble positions for diastole, and on
453 (N=44, N=102, N=199, N=199, N=147, N=85) bubble trajectories representing respectively (259, 725,
454 1746, 1700, 1276, 539) bubble positions for systole. For the 62.5 μm bins (5 bins), speed differences
455 were estimated on (N=56, N=69, N=93, N=11, N=128) bubble trajectories representing respectively
456 (213, 301, 401, 510, 525) bubble positions for the diastole, and on (N=44, N=59, N=65, N=90, N=110)
457 bubble trajectories representing respectively (173, 206, 230, 364, 528) bubble positions for the systole.
458 Finally for the 25 μm bins (5 bins), speed differences were estimated on (N=46, N=51, N=64, N=67,
459 N=74) bubble trajectories representing respectively (150, 122, 173, 216, 233) bubble positions for the
460 diastole,

461 ***Animated flow rendering and supplemental video***

462 Computed-generated imagery (CGI) animation (supplementary material) was created using the
463 software Houdini 17.5.360 (SideFX, Toronto, Canada) to help visualizing functional information
464 extracted from bubble positions and tracking information. Density map and velocity vector
465 components V_x , V_z were imported into Houdini. A particle distribution was initialized with a particle
466 density proportional to the local bubble density. Then, particle position, size, color and life duration
467 are updated for each frame based on the velocity vector field and local density. Depending on the field
468 of view of the highlighted area, particles were constantly emitted at a rate of 10^4 to 10^5 particles. s^{-1}
469 with a lifetime of 3 seconds. Particle size was made proportional to the measured local microbubbles
470 density for better visualization, meaning that a particle passing by a region with local high density
471 appears bigger than a particle moving through a less dense area. Color of the particles were either
472 based on 1/ the density color map (black to red to yellow color map) or 2/ the velocity colormap (blue
473 to green to yellow to red map).

474 Finally, animation was rendered using the “3D renderer Mantra” library of Houdini software after
475 setting-up an additional dome light effect.

476 ***Clinical imaging***

477 The clinical image of Figure 2a,c is a mean intensity projection (MIP) reconstruction from a cerebral
478 multi detector computed tomography (MDCT) cerebral **angiogram** with contrast injection. The clinical
479 image of Figure 4b and suppl Figure 6(top) are cerebral multi detector computed tomography (MDCT)
480 with contrast injection illustrating a sacciforme aneurysm of the right M1-M2. The clinical image of
481 Figure 4c and suppl Figure 6 (bottom) corresponds to axial and mean intensity projection (MIP)
482 reconstructions of a time-of-flight (TOF) MR angiography of the circle of Willis illustrating the same
483 lesion. Figure 4h and suppl Figure 7 are Time-of-flight (TOF) MR angiography of the circle of Willis. Note
484 the moyo-moya pattern of the left middle cerebral artery M1 segment. Dominant right A1 segment
485 and fetal origin of left PCA as normal variants.

486 ***Data availability***

487 Data supporting the findings associated with the figures of this study are available upon
488 request. Example data can be downloaded in the supplementary materials of the publication
489 on a repository website.

490

491 ***Author contributions***

492 C.D., F.P. and M.T. conceived the study; C.D., J.R. and M.P. developed the sequence
493 acquisitions and beamforming software; C.D., J.R. and F. P. acquired data; C.D., J.R., B.H., A.

494 D., M. P and M.T. developed data processing algorithms. A.D. and C. D. developed the
495 visualization algorithms. C.D., F.P. and M.T. interpreted the results. C.D. and M.T. wrote the
496 first draft of the manuscript with substantial contribution from F.P. All authors edited and
497 approved the final version of the manuscript.

498 **Competing interests**

499 M.P. and M.T are co-founders and shareholders of Iconeus company commercializing
500 ultrasound neuroimaging scanners.

501

502 **References**

- 503 1. Liesz, A. The vascular side of Alzheimer's disease. *Science* **365**, 223–224 (2019).
- 504 2. O'Brien, J. T. & Thomas, A. Vascular dementia. *The Lancet* **386**, 1698–1706 (2015).
- 505 3. Betzig, E. *et al.* Imaging Intracellular Fluorescent Proteins at Nanometer Resolution. *Science* **313**,
506 1642–1645 (2006).
- 507 4. Rust, M. J., Bates, M. & Zhuang, X. Sub-diffraction-limit imaging by stochastic optical reconstruction
508 microscopy (STORM). *Nat. Methods* **3**, 793–796 (2006).
- 509 5. Errico, C. *et al.* Ultrafast ultrasound localization microscopy for deep super-resolution vascular
510 imaging. *Nature* **527**, 499–502 (2015).
- 511 6. Couture, O., Hingot, V., Heiles, B., Muleki-Seya, P. & Tanter, M. Ultrasound localization microscopy
512 and super-resolution: A state of the art. *IEEE Trans. Ultrason. Ferroelectr. Freq. Control* **65**, 1304–
513 1320 (2018).
- 514 7. Couture, O., Besson, B., Montaldo, G., Fink, M. & Tanter, M. Microbubble ultrasound super-
515 localization imaging (MUSLI). in *2011 IEEE International Ultrasonics Symposium* 1285–1287 (2011).
516 doi:10.1109/ULTSYM.2011.6293576.
- 517 8. Viessmann, O. M., Eckersley, R. J., Christensen-Jeffries, K., Tang, M. X. & Dunsby, C. Acoustic super-
518 resolution with ultrasound and microbubbles. *Phys. Med. Biol.* **58**, 6447–6458 (2013).
- 519 9. Siepmann, M., Schmitz, G., Bzyl, J., Palmowski, M. & Kiessling, F. Imaging tumor vascularity by
520 tracing single microbubbles. in *2011 IEEE International Ultrasonics Symposium* 1906–1909 (2011).
521 doi:10.1109/ULTSYM.2011.0476.

- 522 10. Demené, C. *et al.* Ultrafast Doppler reveals the mapping of cerebral vascular resistivity in
523 neonates. *J. Cereb. Blood Flow Metab.* (2014) doi:10.1038/jcbfm.2014.49.
- 524 11. Demene, C. *et al.* Functional ultrasound imaging of brain activity in human newborns. *Sci.*
525 *Transl. Med.* **9**, eaah6756 (2017).
- 526 12. Demené, C., Mairesse, J., Baranger, J., Tanter, M. & Baud, O. Ultrafast Doppler for neonatal
527 brain imaging. *NeuroImage* **185**, 851–856 (2019).
- 528 13. Imbault, M., Chauvet, D., Gennisson, J.-L., Capelle, L. & Tanter, M. Intraoperative Functional
529 Ultrasound Imaging of Human Brain Activity. *Sci. Rep.* **7**, (2017).
- 530 14. Soloukey, S. *et al.* Functional Ultrasound (fUS) During Awake Brain Surgery: The Clinical
531 Potential of Intra-Operative Functional and Vascular Brain Mapping. *Front. Neurosci.* **13**, (2020).
- 532 15. Bamber, J. C. Attenuation and Absorption. in *Physical Principles of Medical Ultrasonics* 93–166
533 (John Wiley & Sons, Ltd, 2005). doi:10.1002/0470093978.ch4.
- 534 16. Tanter, M., Thomas, J.-L. & Fink, M. Time reversal and the inverse filter. *J. Acoust. Soc. Am.*
535 **108**, 223–234 (2000).
- 536 17. Zhu, Q. & Steinberg, B. D. Large-transducer measurements of wavefront distortion in the
537 female breast. *Ultrason. Imaging* **14**, 276–299 (1992).
- 538 18. Anderson, M. E., McKeag, M. S. & Trahey, G. E. The impact of sound speed errors on medical
539 ultrasound imaging. *J. Acoust. Soc. Am.* **107**, 3540–3548 (2000).
- 540 19. Fry, F. J. & Barger, J. E. Acoustical properties of the human skull. *J. Acoust. Soc. Am.* **63**, 1576–
541 1590 (1978).
- 542 20. Schneider, M. Characteristics of SonoVue™. *Echocardiography* **16**, 743–746 (1999).
- 543 21. Tanter, M. & Fink, M. Ultrafast imaging in biomedical ultrasound. *IEEE Trans. Ultrason.*
544 *Ferroelectr. Freq. Control* **61**, 102–119 (2014).
- 545 22. Papadacci, C., Pernot, M., Couade, M., Fink, M. & Tanter, M. High-contrast ultrafast imaging of
546 the heart. *IEEE Trans. Ultrason. Ferroelectr. Freq. Control* **61**, 288–301 (2014).

- 547 23. compendium.ch. <https://compendium.ch/fr/product/115837-sonovue-subst-seche-c->
548 solv/mpro.
- 549 24. Demene, C. *et al.* Spatiotemporal clutter filtering of ultrafast ultrasound data highly increases
550 Doppler and fUltrasound sensitivity. *IEEE Trans. Med. Imaging* **PP**, 1–1 (2015).
- 551 25. Flax, S. W. & O'Donnell, M. Phase-aberration correction using signals from point reflectors and
552 diffuse scatterers: basic principles. *IEEE Trans. Ultrason. Ferroelectr. Freq. Control* **35**, 758–767
553 (1988).
- 554 26. Prada, C., Wu, F. & Fink, M. The iterative time reversal mirror: A solution to self-focusing in the
555 pulse echo mode. *J. Acoust. Soc. Am.* **90**, 1119–1129 (1991).
- 556 27. Tinevez, J.-Y. *A simple particle tracking algorithm for MATLAB that can deal with gaps.:*
557 *tinevez/simpletracker*. (2019).
- 558 28. Szabo, T. L. *Diagnostic ultrasound imaging: inside out*. (Elsevier Academic Press, 2004).
- 559 29. Paszkowiak, J. J. & Dardik, A. Arterial Wall Shear Stress: Observations from the Bench to the
560 Bedside: *Vasc. Endovascular Surg.* (2016) doi:10.1177/153857440303700107.
- 561 30. Febina, J., Sikkandar, M. Y. & Sudharsan, N. M. Wall Shear Stress Estimation of Thoracic Aortic
562 Aneurysm Using Computational Fluid Dynamics. *Comput. Math. Methods Med.* **2018**, 7126532
563 (2018).
- 564 31. Goudot, G. *et al.* Wall Shear Stress Measurement by Ultrafast Vector Flow Imaging
565 for Atherosclerotic Carotid Stenosis. *Ultraschall Med. Stuttg. Ger.* **1980** (2019) doi:10.1055/a-1060-
566 0529.
- 567 32. Scott, R. M. & Smith, E. R. Moyamoya disease and moyamoya syndrome. *N. Engl. J. Med.* **360**,
568 1226–1237 (2009).
- 569 33. Lee, C.-H., Jeon, S.-H., Wang, S.-J., Shin, B.-S. & Kang, H. G. Factors associated with temporal
570 window failure in transcranial Doppler sonography. *Neurol. Sci.* **41**, 3293–3299 (2020).
- 571 34. Heiles, B. *et al.* Ultrafast 3D Ultrasound Localization Microscopy using a 32×32 Matrix Array.
572 *IEEE Trans. Med. Imaging* 1–1 (2019) doi:10.1109/TMI.2018.2890358.

- 573 35. Morel, D. Human pharmacokinetics and safety evaluation of SonoVue, a new contrast agent
574 for ultrasound imaging. *Invest. Radiol.* 80–85 (2000).
- 575 36. Martin, K. The acoustic safety of new ultrasound technologies. *Ultrasound* **18**, 110–118 (2010).
- 576 37. Bigelow, T. A. *et al.* The thermal index. *J. Ultrasound Med.* **30**, 714–734 (2011).
- 577 38. Gateau, J. *et al.* Transcranial Ultrasonic Therapy Based on Time Reversal of Acoustically
578 Induced Cavitation Bubble Signature. *IEEE Trans. Biomed. Eng.* **57**, 134–144 (2010).
- 579 39. O'Reilly, M. A. & Hynynen, K. A super-resolution ultrasound method for brain vascular
580 mapping. *Med. Phys.* **40**, (2013).
- 581 40. Soulioti, D. E., Espíndola, D., Dayton, P. A. & Pinton, G. F. Super-Resolution Imaging Through
582 the Human Skull. *IEEE Trans. Ultrason. Ferroelectr. Freq. Control* **67**, 25–36 (2020).
- 583 41. Kasai, C., Namekawa, K., Koyano, A. & Omoto, R. Real-time two-dimensional blood flow
584 imaging using an autocorrelation technique. *IEEE Trans Sonics Ultrason* **32**, 458–464 (1985).
- 585 42. Bercoff, J., Tanter, M. & Fink, M. Supersonic shear imaging: a new technique for soft tissue
586 elasticity mapping. *IEEE Trans. Ultrason. Ferroelectr. Freq. Control* **51**, 396–409 (2004).
- 587 43. Jerman, T., Pernuš, F., Likar, B. & Špiclin, Ž. Enhancement of Vascular Structures in 3D and 2D
588 Angiographic Images. *IEEE Trans. Med. Imaging* **35**, 2107–2118 (2016).
- 589 44. Jerman, T., Pernuš, F., Likar, B. & Špiclin, Ž. Beyond Frangi: an improved multiscale vesselness
590 filter. in *Medical Imaging 2015: Image Processing* vol. 9413 94132A (International Society for Optics
591 and Photonics, 2015).
- 592 45. Frangi, A. F., Niessen, W. J., Hoogeveen, R. M., Van Walsum, T. & Viergever, M. A. Model-based
593 quantitation of 3-D magnetic resonance angiographic images. *IEEE Trans. Med. Imaging* **18**, 946–
594 956 (1999).
- 595 46. Hingot, V. *et al.* Microvascular flow dictates the compromise between spatial resolution and
596 acquisition time in Ultrasound Localization Microscopy. *Sci. Rep.* **9**, 2456 (2019).
- 597 47. Errico, C. *et al.* Transcranial functional ultrasound imaging of the brain using microbubble-
598 enhanced ultrasensitive Doppler. *NeuroImage* **124, Part A**, 752–761 (2016).

599

600

601

602 **Acknowledgements**

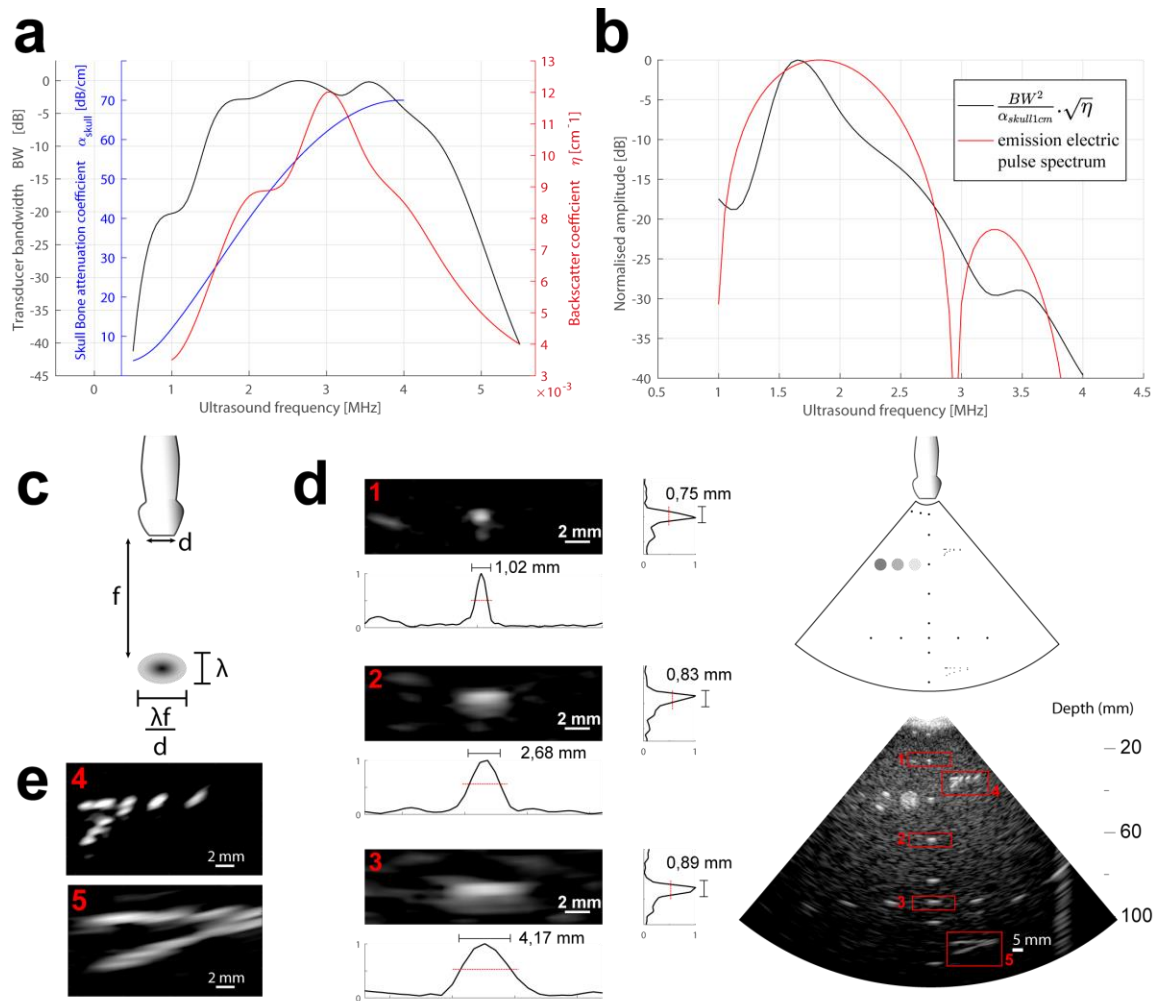
603 This work was supported by a research grant from the European Research Council (ERC) under the
604 European Union's Seventh Framework Program (FP7/2007–2013)/ERC Advanced grant agreement no.
605 339244-FUSIMAGINE, by the Swiss National Foundation (Fond National Suisse) grant n°
606 CR3213_150654 (F Perren), and the Fondation Bettencourt-Schueller.

607 The authors thank Liene Puke for her help recruiting the patients. The authors thank the NVIDIA
608 Corporation for their support through the NVidia GPU Grant program and the donation of a Titan Xp
609 GPU used for this research.

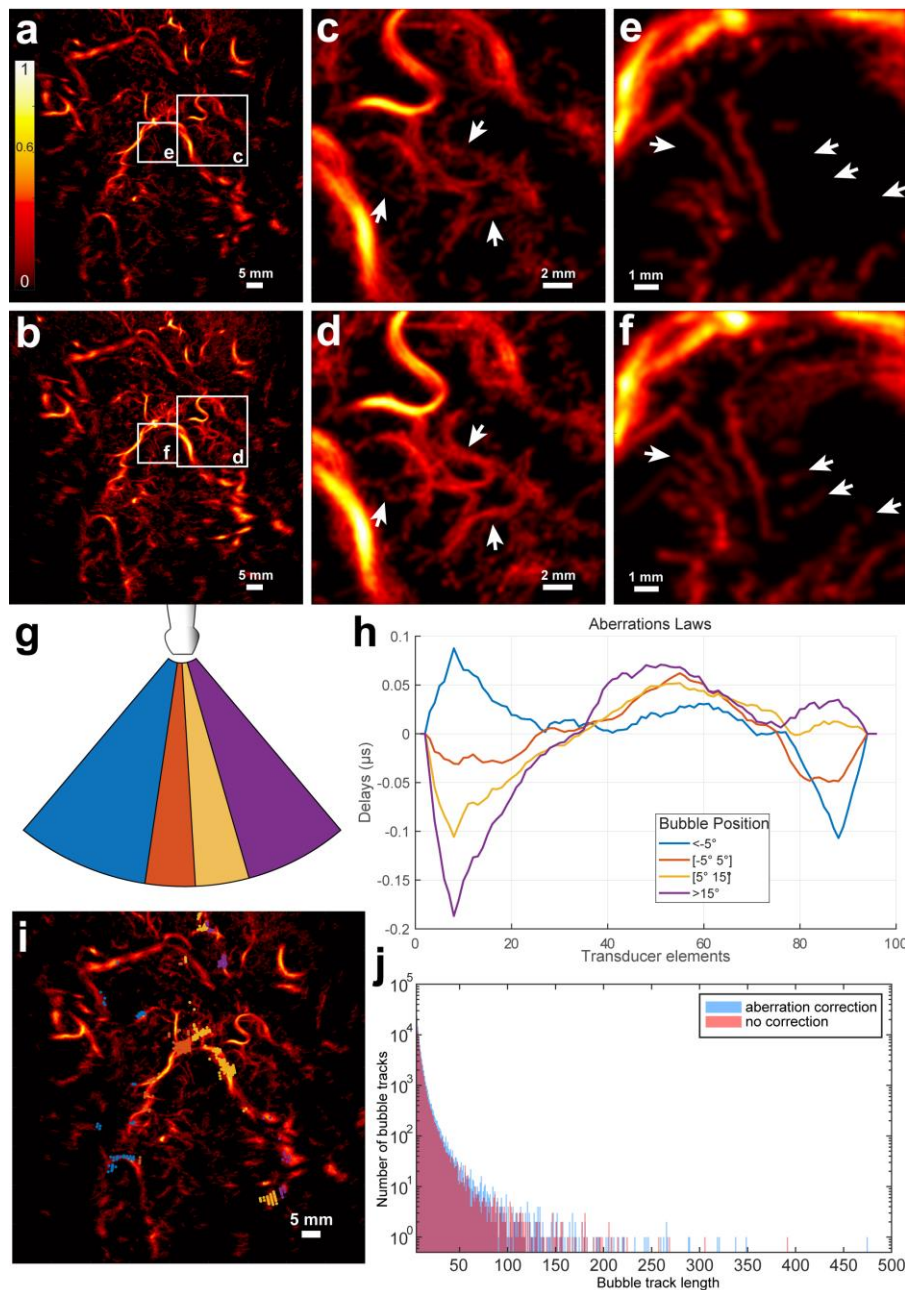
610

611

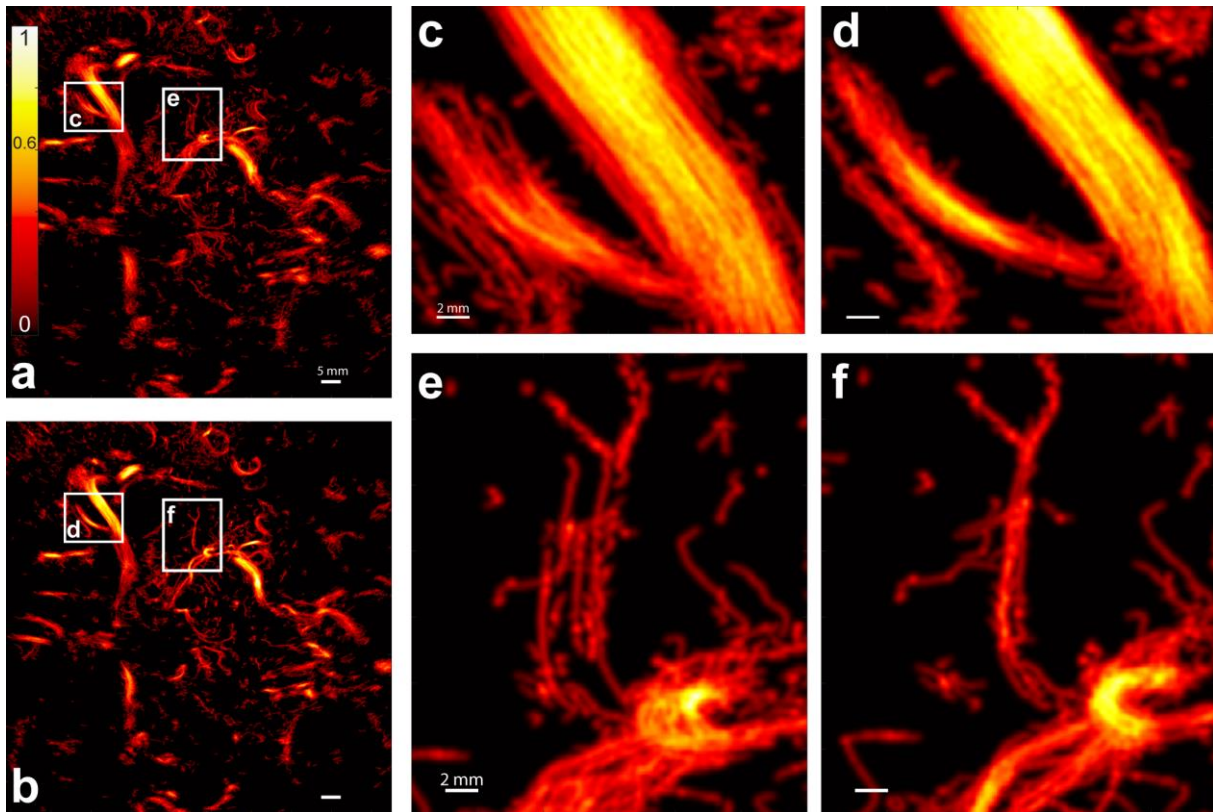
Accepted manuscript, Confidential



Suppl. Fig. 1 : Choice of the emission frequency and effect on the diffraction-limited resolution of the ultrasonic probe used in the study. **a.** Choice of the emission frequency is influenced by the available transducer bandwidth (black), the skull bone attenuation (blue) and the power of the backscattering of the Sonovue® microbubbles (red). **b.** Combining these parameters gives a relatively narrow window between 1.5 and 2 MHz for t-ULM (black). The frequency spectrum (red) of the electric pulse used to drive the ultrasound transducer targets this peak. **c.** Axial resolution is roughly equal to the wavelength λ (with a two-cycles emission pulse), therefore loss of axial resolution with depth is low, and can be attributed to higher attenuation of the high frequency content, resulting in a slightly longer ultrasound pulse at depth. Lateral resolution is given both by the wavelength λ and by the aperture (characterized by the f-number f/d) of the ultrasound probe, and is commonly accepted as being given by $\lambda f/d$, where f is the focal distance (i.e. the depth), and d the width of the probe (the aperture). The lateral resolution can be up to 6 mm at a depth of 12 cm in our case. **d.** Point spread function (PSF) evaluation based on the imaging of a subwavelength point target at depths of 20 mm (1), 58mm (2), and 88mm (3). These PSF are obtained on a calibrated imaging phantom containing subwavelength ($\varnothing = 80 \mu\text{m}$) strings invariant along the elevation direction. **e.** Resolution limit at 30 mm (4) and 110 mm (5) depths. At 30 mm, the 2 closest couples of point targets, being 250 and 500 μm apart, are not distinguishable neither in the axial or lateral dimension. At 110 mm, axial resolution is more or less conserved, and lateral resolution is so degraded that only the targets that are 4 and 5 mm apart can be distinguished.



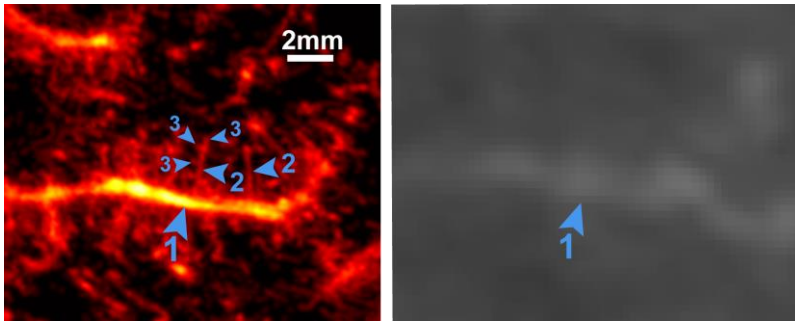
Suppl. Fig. 2 : Correction of the aberrations induced by transcranial propagation : ULM image **a.** with and **b.** without applying the aberration correction and adaptive beamforming of the ultrasonic raw data. Color bar applies for all t-ULM images. **c.** Without aberration correction some vessels appear fuzzy, as the loss of intensity due to distorted reception focusing leads the t-ULM algorithms to lose track of bubbles (arrows) **d.** Those vessels are recovered using aberration corrections as described in the M & M section. **e.** Without aberration correction small vessels may also be completely missed due to loss of intensity or distorted psfs (arrows). **f.** Correcting for the aberrations enables to track those previously invisible bubbles (arrows). **g.** Positions of the isoplanetic patches used for this acquisition, one aberration correction is derived for each patch. **h.** Aberration law for each isoplanetic patch. **i.** Position of the bubbles used for determination of the aberration laws. **j.** Count of the number of bubble tracks detected vs the length of the bubble track (expressed in number of imaging frames: 400 frames equals 0.5 s). The effect of the aberration correction is two-fold: more bubbles are detected and longer tracks are identified, as correcting for the distorted focusing prevents the splitting of long tracks into smaller one that can be due to temporary loss of the bubble position.



614

615 **Suppl. Fig. 3:** Motion correction effect on the 24 s of acquisition of t-ULM in the patient of Figure 4a.
 616 **a.** t-ULM image without motion correction. Color bar applies for all ULM images. White boxes depicts
 617 zooms in c and e. **b.** t-ULM image with motion correction. White boxes depicts zooms in c and e. **c.**
 618 Without motion correction the big vessel section is larger and the two small vessels cannot be
 619 distinguished when comparing with d. **d.** with motion correction. **e.** Without motion correction the
 620 individual bubble trajectories occurring at different moments in time are scattered and prevent the
 621 visualisation of this small branching vessel observed in f. **f.** With motion correction.

622

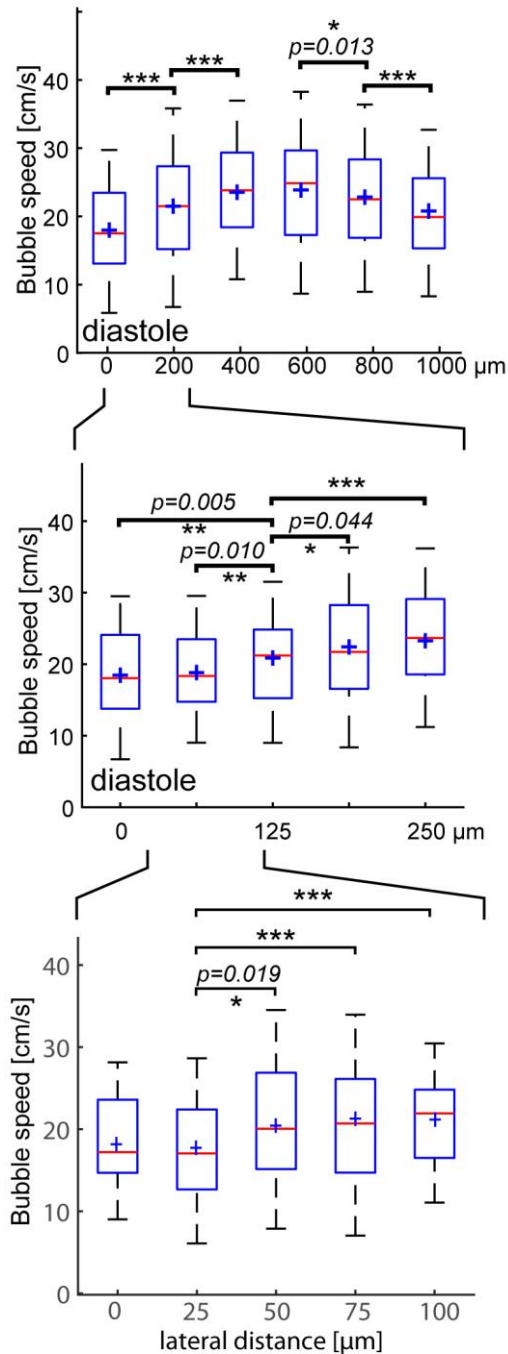


623

624 **Suppl. Fig. 4:** Vessel branching in figure 2, detail. We can see that vessel 1 is visible both on t-ULM and
625 CT, but that branching order 2 and 3 can only be seen on t-ULM.

626

Accepted manuscript, Confidential

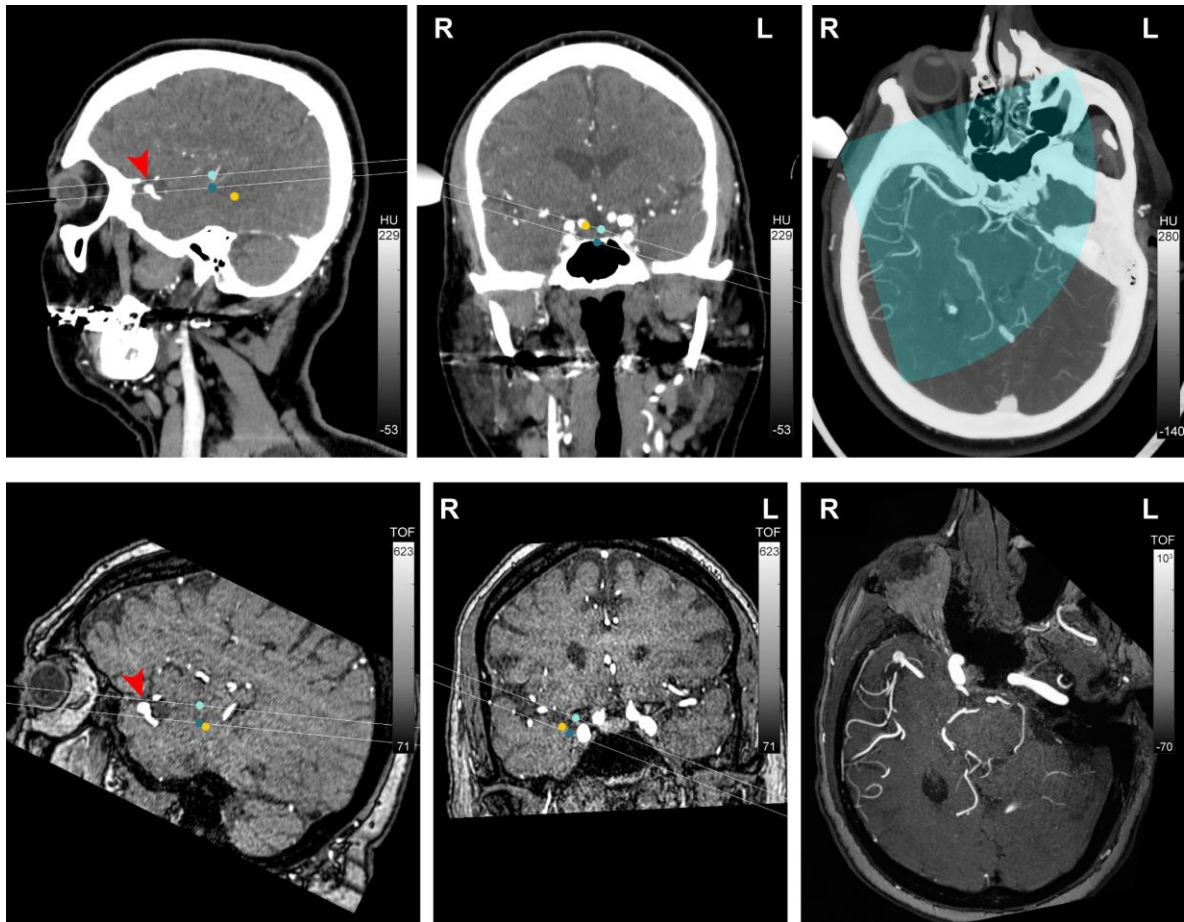


627

628 **Suppl Fig 5:** Minimal resolution achievable in the experimental conditions used in this study appears
 629 to be 25 μm (significant difference between bubble speed bins number 2 and 3 on the bottom box
 630 plot), estimated when considering the bubble speeds near the edge of the vessel of Figure 3. This was
 631 estimated in diastole, as the number of bubbles is higher (larger temporal extent) and the distribution
 632 of microbubble speeds is more narrow. Red central line indicates the median; boxes, 25th and 75th
 633 percentile; whiskers are ± 1.26 σ corresponding to 80% coverage in the Gaussian hypothesis (blue cross
 634 represents mean value). Significant differences in the mean value have been tested with p < 0.05 (*),
 635 p < 0.01 (**) and p < 0.001 (***), Analysis of variance (ANOVA) with post hoc t-test with Bonferroni
 636 correction. The 2 top boxplots are the same than the ones displayed on figure 3e and 3f (diastole).
 637 The bottom boxplot depicts the 25μm binning, mean and variance (in mm/s) and samples number
 638 (bubble positions) corresponding from left to right bins : 182+/-68 (N=150); 177+/-68 (N=122); 204+/-

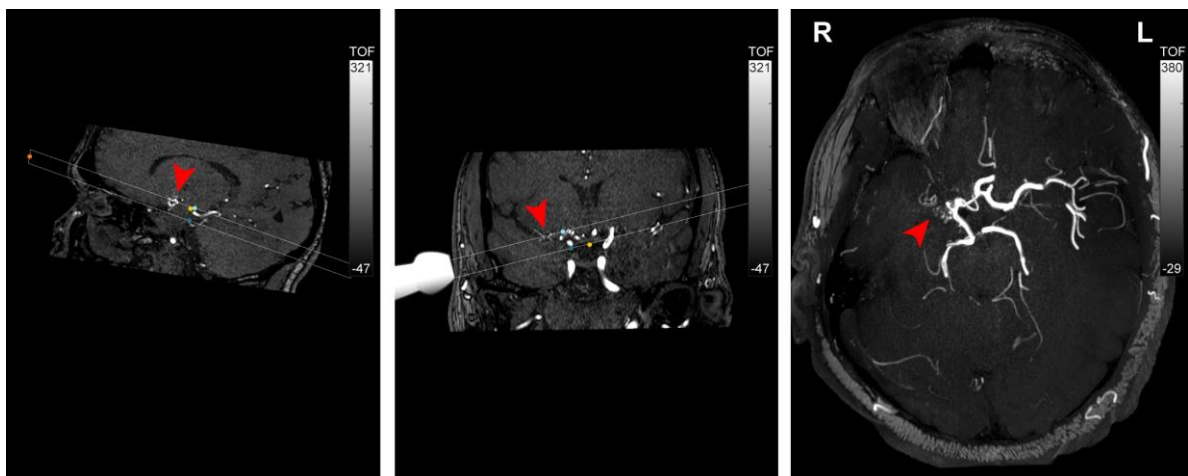
639 79 (N=173); 213+/-78 (N=216); 212+/-72 (N=233); (p-values are: (2-3) 0.019, (2-4) $2.4 \cdot 10^{-4}$, (2-5) $3.2 \cdot 10^{-4}$).

Accepted manuscript, Confidential



Suppl. Fig. 6 : CTA (top, Color bar in Hounsfield) and MRA (bottom, Color bar in arbitrary units) images for the patient in Figure 3a to 3e. Aneurysm is depicted by the red arrowhead. The ultrasonic imaging plane is represented as a slab, which is thicker than the real ultrasonic imaging plane thickness, with the latter being uneven with depth. Ultrasonic field of view is depicted as light blue overlay on the CT image. Right images are maximum intensity projection of that slab in each case.

641



Suppl. Fig. 7 : MRA (Time of Flight) (Color bar in arbitrary units) images for the patient in Figure 3f to 3i. Network of collaterals is depicted by the red arrowhead. Right image is a maximum intensity projection of the slab depicted on the two images at left.